Highlights

- Effects of heat-treatment on the initial stages of oxidation are studied at 650 °C
- Age-precipitation of Laves phase blocks the fast diffusion of Mn to the oxide scale
- Interfacial Si oxidation at different precipitates is followed in real time

High-temperature oxidation of ferritic stainless steel

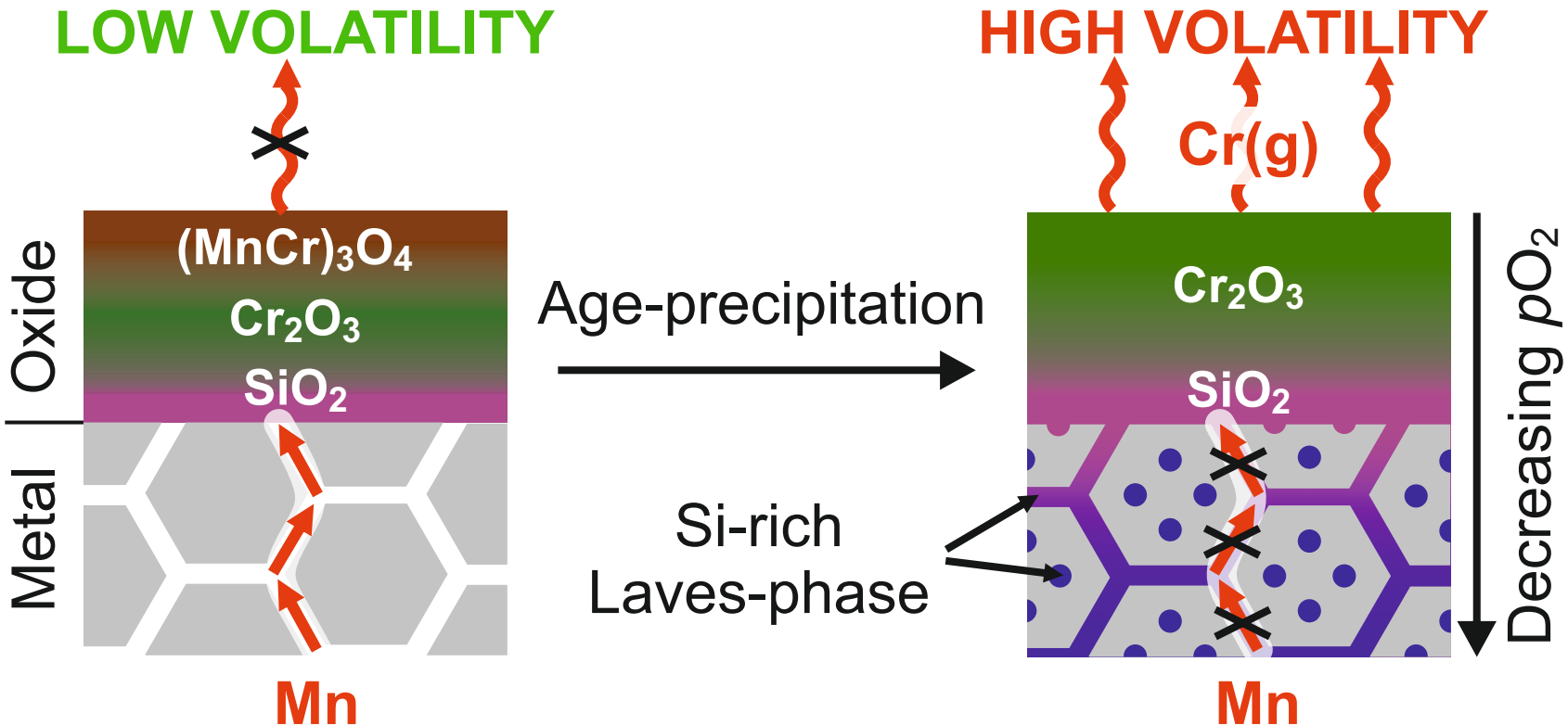

The role of $(FeCrSi)_2(MoNb)$-type Laves phase on the formation of Mn-rich protective oxide scale on ferritic stainless steel

Harri Ali-Löytty[a], Markku Hannula[a], Timo Juuti[b], Yuran Niu[c], Alexei A. Zakharov[c], and Mika Valden[a,*]

[a]Surface Science Group, Laboratory of Photonics, Tampere University of Technology, P.O. Box 692, FI-33101 Tampere, Finland

[b]Centre for Advanced Steels Research, University of Oulu, P.O.B. 4200, FI-90014 Oulu, Finland

[c]MAX IV Laboratory, Lund University, P.O. Box 118, SE-22100 Lund, Sweden

[*]To whom correspondence should be addressed. Tel.: +358 40 849 0261. E-mail address: mika.valden@tut.fi (M. Valden).

Abstract

Microalloying of stainless steel with reactive elements increases oxidation resistance but makes the alloy prone to microstructural changes. XPS results reveal changes in the initial oxidation mechanism on Ti–Nb stabilized ferritic stainless steel (EN 1.4521) after 120 h heat treatment at 650 °C. Age-precipitation of $(FeCrSi)_2(MoNb)$-type Laves phase resulted in less pronounced surface segregation and oxidation of microalloying elements. Si oxidizes preferentially at the Laves precipitate locations via outward diffusion forming diffusion barrier for the other scale forming elements. Most significantly the diffusion of Mn and the formation of low volatile $(Mn,Cr)_3O_4$ spinel oxide at the surface was strongly suppressed.

Keywords: A. stainless steel; B. XPS; C. interfaces; C. segregation; C. oxidation

1. Introduction

High-temperature corrosion resistance of ferritic stainless steels (FSSs, Fe–Cr based alloys) is built upon the formation of protective oxide scale consisting of Cr_2O_3-based outer layer and amorphous SiO_2 at the scale/alloy interface [1]. Unfortunately, Cr_2O_3 reacts with oxygen and water releasing Cr vapors, which eventually leads to corrosion under moist high-temperature operation conditions [2,3]. In particular, Cr vaporization has been identified as the most significant failure mechanism in solid-oxide fuel cells (SOFCs) limiting the use of FSSs as interconnect material [4].

In SOFC applications Cr volatilization has been mitigated by coating FSS interconnects with a layer of Cr-free spinel oxide, for example, $(Mn,Co)_3O_4$. Alternatively, it is possible to reduce Cr_2O_3 activity by alloying steel with < 1 wt.% Mn that induces the formation of low volatile Mn-rich $(Mn,Cr)_3O_4$ spinel oxide on top of the Cr_2O_3 during the early stages of oxidation [5]. Thus, the development of alloys that form protective oxide scale under specific corrosive environment requires careful analysis of oxidation mechanism and optimization of alloying additions [6–8].

Increasing degree of alloying makes the steel prone to the precipitation of secondary phases such as carbonitrides and intermetallic Laves phases (e.g., Fe_2Nb) [7,9], which can affect both the mechanical and surface properties. Similar to high-temperature oxidation also secondary phase formation involves diffusion processes that are strongly influenced by the temperature. Therefore, it is of utmost importance to test material properties at the correct application temperature. SOFCs typically operate between 600–800 °C [10,11], albeit there

is a strong demand to lower the operation temperature below 500 °C [12,13]. Such a temperature range is rather wide in terms of material selection and alloy development. Regarding oxidation, at 800 °C high-Cr FSSs form protective Cr_2O_3 oxide scale but at temperatures below 600 °C the diffusion of Cr is not necessary sufficient and Fe-rich non-protective oxide scale can form instead [14]. Moreover, we recently showed that the segregation of microalloying elements (Si, Nb, Ti) initiates at ~550 °C and is strongly temperature dependent [15]. In terms of secondary phase formation, the stability and composition of secondary phase particles depend on the temperature, for example, Niewolak et al. showed that Si content of Laves phase was nearly doubled when temperature was decreased from 800 to 700 °C [16]. Incorporation of Si into the Laves phase increases the electrical conductivity of the oxide scale which is an advantage in SOFC interconnect application [17].

Dislocations and grain boundaries provide favorable nucleation sites for secondary phase particles but are also fast diffusion paths for oxide scale forming elements, in particular, Cr and Mn [18]. The precipitation of Laves phase at these defects has been suggested to hinder the diffusion along the fast diffusion paths, and may affect the oxide scale growth mechanism and composition [19]. The diffusion of Mn in Cr_2O_3 is about two orders of magnitude faster than Cr, and therefore, Mn-rich oxide forms during the early stages of oxidation at the surface [20]. On the contrary, diffusion through amorphous SiO_2 that forms at the oxide scale/alloy interface is kinetically constrained which reduces the oxidation rate [1].

In the present study, we show a change in the initial oxidation mechanism at 650 °C on Ti–Nb stabilized FSS (EN 1.4521) upon 120 h heat treatment at 650 °C. The X-ray photoelectron spectroscopy (XPS) analysis of surface segregation and oxidation under controlled ultra-high vacuum (UHV) conditions reveal that age-precipitation of $(FeCrSi)_2(MoNb)$-type Laves phase results in reduced surface segregation and oxidation of minor alloying elements. The use of synchrotron radiation mediated photoemission electron microscopy (PEEM) allowed us to follow oxide film formation in real time on individual precipitates at low pO_2. The results show that Si oxidizes preferentially at the Laves precipitate locations via fast outward diffusion forming a diffusion barrier for the subsequent growth of oxide scale. Most significantly the diffusion of Mn and formation of low volatile $(Mn,Cr)_3O_4$ spinel oxide at the surface was compromised.

2. Experimental

The investigated EN 1.4521 ferritic stainless steel was supplied by Outokumpu Stainless Oy (Tornio, Finland). The bulk composition and calculated equilibrium composition at 650 °C for the investigated steel are shown in Table 1. The equilibrium composition was determined by the Thermo-Calc® software and TCFE7 database. Disk-shaped samples (1 mm thick, diameter of 9 mm) were cut from a cold rolled, heat treated, pickled and skin passed sheet (i.e. 2B surface finish). The first sample was initially aged in an Ar atmosphere at 650 °C for 120 h in order to induce precipitation of the $(FeCrSi)_2(MoNb)$-type Laves phase. The sample, denoted as "AGED" in the results below, was then water quenched and polished to mirror finish prior to analysis. Before polishing, the heat-tint

oxide and Cr/Mn-depleted layer were removed by grinding, and the glow discharge optical emission spectroscopy (GDOES) analysis was applied to verify that the elemental composition had not changed upon the heat treatment. The microstructure of the AGED sample was previously reported in Ref. [21]. Another sample without any heat treatments, denoted as "NOT-AGED", was grinded and polished to mirror finish before analysis.

Oxidation experiments in ambient air were carried out *ex situ* by placing the samples directly into a tube furnace at 650 °C for 30 min. Then the samples were removed from the furnace and let to cool down freely followed by the PEEM analysis and XPS depth profiling.

Oxidation experiments at low pO_2 were carried out *in situ* in two separate surface analysis systems under controlled UHV atmosphere with base pressures below 1×10^{-8} Pa. After loading the samples into the system, atmospheric impurities and native oxides were first removed by cycles of 2.0 keV Ar^+ ion sputtering at 25 °C and subsequent flash annealing at 800 °C. After the final sputtering cycle before an oxidation experiment the sample was annealed at 650 °C for 5 min. Oxidation experiments were then carried out by backfilling the chamber with 5.3×10^{-7} – 5.3×10^{-5} Pa of O_2 (99.9999%) for 250 – 2500 s while maintaining the sample at the oxidation temperature of 650 °C. The chemical composition of the surface was subsequently analyzed by XPS, X-ray absorption spectroscopy PEEM (XAS-PEEM) and PEEM at 25 °C with the exception of an *operando* experiment. During the *operando* experiment PEEM data was recorded in real time while maintaining the

sample at 650 °C under the oxygen pressure of 5.3×10^{-7} Pa. For experimental details on surface analytical equipment, data acquisition and analysis see Supplementary material.

3. Results and discussion

3.1. Age-precipitation of EN 1.4521 at 650 °C

SE image in Fig. 1(a) shows the surface of the AGED sample after polishing, i.e. the microstructure of the bulk sample, indicating the presence of different types of precipitated particles. XAS-PEEM images of Nb and Ti in Figs. 1(b) and (c), respectively, reveal the inhomogeneous distribution of these microalloying elements.

Highly stable Ti(CN)- and (NbTi)C-type particles were present in the alloy in the as-received condition originating from the conventional industrial processing stages of the alloy. The big Ti(CN) particle in Fig. 1 is surrounded by (NbTi)C particles. In addition to Ti(CN) and (NbTi)C particles, small (< 1 μm in diameter) $(FeCrSi)_2(MoNb)$-type Laves phase particles were observed. A small fraction of tiny Laves phase particles were present in the as-received sample but the number density and the size of Laves particles increased substantially upon heat treatment at 650 °C for 120 h. Other second phase particles were not observed. Furthermore, the heat treatment did not cause grain size coarsening from an average grain diameter of 20 μm, see Ref. [21] for more detailed discussion.

The Laves phase nucleation in bcc Fe alloys has been observed to occur first at the grain boundaries, then on dislocations and finally in the matrix [22]. The Laves particles in Fig. 1(a) are randomly distributed on the surface suggesting that also narrow grain boundaries

and dislocations contain Laves phase. Indeed, Juuti et al. confirmed the nucleation of Laves phase at the grain boundaries [21].

The calculated equilibrium mole fraction of the Laves phase at 650 °C for the investigated steel is 0.68 at.% (Table 1), and the Laves phase dissolves at temperatures above 800 °C. The calculated composition of the Laves phase at 650 °C in atomic-% is 57.7%Fe–2.0%Cr–6.9%Si–7.6%Mo–25.8%Nb. In addition, the calculation showed that the Laves phase contains trace amounts of Ti (0.02 at.%) and Ni (0.02 at.%), and in particular, that there is no Mn (< 0.001 at.%). It is worth mentioning that the mole fraction of Laves phase is proportional to the total amount of Nb and Mo, and therefore, EN 1.4521 alloy is more susceptible to Laves phase precipitation than, for example, EN 1.4509 with almost the same composition but without Mo.

The similar Nb and Ti distributions in Fig. 1(b) and (c) XAS-PEEM images corroborate that Laves particles contain significant amount of Ti, albeit only trace amounts well below the bulk concentration (0.14 at.%) were expected based on the calculation. Also, Niewolak et al. have showed using atom probe analysis (APT) the incorporation of Ti into a $(FeCrSi)_2Nb$-type Laves phase and suggested that Ti may affect the Laves phase nucleation [16]. Using the same method Isik et al. showed that precipitation of Mo-rich Laves phase in 12 wt.% Cr tempered martensite ferritic steel (TMFS) preceded combined segregation of Mo, Si and P to the grain boundaries, where Laves phase nucleation was initiated next to $M_{23}C_6$ carbides [23]. Our surface segregation experiments on metallic surface confirm that P segregates to a metallic surface at 650 °C (not shown). In contrast to the carbide hardened

TMFS material with 0.9 at.% of C, the studied EN 1.4521 (0.06 at.% C) had no carbides at the grain boundaries that could have directed the nucleation of Laves particles.

3.2. Oxide film formation under ambient air conditions

The influence of Laves-phase precipitation on the oxide scale chemical composition was first studied in ambient air (high pO_2). Fig. 2 shows XPS surface analysis of NOT-AGED and AGED EN 1.4521 after oxidation in air at 650 °C for 30 min. The most striking difference between the two samples can be seen from the Mn 2p spectra depicted in Fig. 2(a). On the NOT-AGED sample the Mn $2p_{3/2}$ peak centered at 641.2 eV corresponds to oxidized $Mn^{2+/3+}$ in either Mn_2O_3, Mn_3O_4 or most likely in $(Mn,Cr)_3O_4$ spinel-type oxide [24,25]. In contrast, on the AGED sample the Mn 2p signal is almost completely absent.

The surface sensitive PEEM images of oxidized Mn, Fe and Cr in Figs. 2(c) and (e) show that oxidized species are homogeneously distributed on the surfaces. None of the species is enriched at the alloy grain boundary locations which can be identified from the SE images in Figs. 2(b) and (d) that were measured at the same positions. Grain boundaries provide fast diffusion paths for scale forming elements, and in particular, strong surface enrichment of Mn has been shown to emanate preferentially through alloy grain boundaries in Fe–Cr alloys with only < 1 wt.% Mn [26]. The homogeneous Mn distribution at the surface of the NOT-AGED sample suggests that the oxide scale grows primarily via outward diffusion of Mn, Fe and Cr. The results are in line with Horita et al. who, using SIMS depth profiling of an Fe–Cr alloy after oxidation at 800 °C for 144 h, observed homogeneous Mn distribution at the oxide scale surface while Mn was enriched at the grain boundaries below the oxide

scale [26]. Also, Magdefrau et al. observed enrichment of both Mn and Cr at the alloy grain boundaries of an Fe–Cr alloy (Crofer 22 APU) after oxidation at 800 °C for 5 h using bulk sensitive EDXS imaging [27].

Fig. 3 shows XPS depth profiles of NOT-AGED and AGED EN 1.4521 after oxidation for 30 min at 650 °C in ambient air. The oxidized and metallic components were separated by their corresponding chemical shifts in the high-resolution XPS spectra.

The oxide scale on the NOT-AGED sample consisted of the Cr and Mn -rich outer scale (possible chemical compound based on XPS peak positions is $(Mn,Cr)_3O_4$), Cr-rich subscale (Cr_2O_3) and oxide/metal interface enriched with Si (SiO_2) and Nb (Nb_2O_5). Such a layered oxide structure is typical of Fe–Cr alloys oxidized at high temperatures [14,17,28]. In addition, significant amount of oxidized Fe (Fe cations can substitute Cr and Mn sites in $(Mn,Cr)_3O_4$ and Cr_2O_3) and some Mo (MoO_3) were present in the outer oxide scale. These species were concluded to be formed due to the high oxidation rate under ambient pressure conditions and are likely to become transformed into the thermodynamically more favorable species, e.g. $(Mn,Cr)_3O_4$ and Cr_2O_3, with increasing oxidation time [24,29,30]. Supporting the statement, no Mo and Fe oxides were observed in oxidation tests at low pO_2 in Chapter 3.3. It is worth mentioning, though, that the oxide scale growth on Fe–Cr alloys at high-temperatures is a diffusion-controlled process, in which temperature is a key parameter determining whether Cr alloying is sufficient to sustain the growth of protective Cr-rich oxide scale or if a non-protective Fe-rich oxide scale forms instead. Young et al. studied oxidation of EN 1.4509 (similar composition with EN 1.4521 but without Mo) in

Ar–H_2–H_2O and showed that the oxide scale composition changed from Fe to Cr -rich when the oxidation temperature was increase from 600 to 650 °C [14]. Thus, it was concluded that the EN 1.4521 had sufficient Cr alloying to form protective Cr-rich oxide scale at 650 °C.

The oxide scale on the AGED sample had similar in-depth distributions for all the other elements except Mn and Cr. Surprisingly, Mn was almost completely absent from the oxide scale. It was noticed that the Cr in-depth distribution on the AGED sample was similar with the combined in-depth distributions of Mn and Cr on the NOT-AGED sample that suggests strongly competing diffusion processes. Furthermore, no significant difference in the oxide scale thicknesses (approximately 40 nm) was observed between the AGED and NOT-AGED samples. Further analysis of oxidation kinetics was beyond the scope of this study.

Recently, we did similar oxidation experiment at 650 °C for EN 1.4509 (no Mo) alloy that forms $(FeCrSi)_2Nb$-type Laves phase [17]. In that study the heat treatment was conducted at higher temperature (800 °C). In sharp contrast to the Mo-alloyed EN 1.4521, the precipitation of $(FeCrSi)_2Nb$ Laves phase within EN 1.4509 did not attenuate Mn diffusion to the oxide scale. It should be noted that EN 1.4521 exhibits higher propensity to form Laves phase, and that the $(FeCrSi)_2(MoNb)$-type Laves phase has approximately 2% smaller lattice parameters than $(FeCrSi)_2Nb$-type Laves phase [21,31]. Furthermore, Juuti et al. showed that the $(FeCrSi)_2(MoNb)$-type Laves phase has lattice parameters similar to Fe_2Mo-type Laves phase, and concluded that the substitutional elements Si and Nb had little effect on the lattice parameters. Also, the difference in heat treatment temperature may

have affected the nucleation mechanism. Laves phase nucleation has been shown to precede the enrichment of Si and P at grain boundaries [23], and the segregation of both elements onto a metallic EN 1.4521 surface has been shown to be strongly temperature dependent [15]. Therefore, the apparent inconsistency is attributed to the differences in Laves phase composition, mole fraction in the alloy, nucleation and lattice parameters. It is likely that smaller sized $(FeCrSi)_2(MoNb)$-type Laves phase can more densely occupy grain boundaries and dislocation, and thus, limit more effectively Mn diffusion to the oxide scale compared to $(FeCrSi)_2Nb$-type Laves phase.

Horita et al. compared oxidation properties between a Laves-phase forming Fe–Cr alloy containing Mo and Nb with a conventional Fe–Cr alloy in reducing H_2-H_2O atmosphere [19], and concluded that the elemental diffusion through the grain boundaries was decreased in the Laves-phase forming alloy. Moreover, the oxide scale depth profiles measured after 1104 h oxidation at 800 °C in Fig. 5 of Ref. [19] reveal smaller Mn concentration in the oxide scale of the Laves phase forming alloy compared to the conventional alloy, regardless of the higher bulk concentration of Mn (0.50 vs. 0.21%). In accordance with Horita et al., the oxidation test under ambient air conditions revealed that the $(FeCrSi)_2(MoNb)$ Laves phase precipitation strongly suppressed the Mn diffusion to the oxide scale, and thus, limited the formation of $(Mn,Cr)_3O_4$ spinel oxide at the surface.

3.3. Initial oxidation at low pO_2

In order to focus on the earlier stages of oxidation, experiments were conducted at low pO_2. This approach allows surface analytical investigation of segregating elements to an alloy

surface while kinetically controlling the oxide formation. The same oxide species are detected in the oxide scale of Fe–Cr alloys under atmospheric air conditions and at pO_2 as low as 10^{-13} Pa [32]. However, the oxidation at low pO_2 favors the formation of thermodynamically most stable oxides, such as oxides of Ti, Si and Nb [17], that comprise the diffusion barrier at the oxide/metal interface. In particular, within the short oxygen exposures, the oxygen induced surface segregation and oxidation of Si overcame the formation of Cr oxides. Therefore, the use of low pO_2 allowed the investigation of initial stages of interfacial Si oxidation before the formation of Cr rich oxide scale on top.

Fig. 4 shows the XP spectra of selected elements for the NOT-AGED and AGED sample after oxygen exposure in 5.3×10^{-5} Pa O_2 for 250 s at 650 °C. The oxygen exposure was selected to emphasize the influence of Laves-phase precipitation on the early stages of oxidation for all the elements that form the oxide scale. Before oxygen exposures, the samples were sputter cleaned and annealed for 5 min at 650 °C in UHV. In addition to the oxidized species presented in Fig. 4, some oxidized Al was detected on both surfaces. In contrast to the oxidation test in ambient air, no oxidized Fe or Mo were detected on either surface (Figs. 4(a) and (d)). Instead, surfaces consisted of oxidized species of Cr, Mn, Nb, Ti and Si (Figs. 4(b), (c), (e), (f), (g)). At the surface of the AGED sample the amounts of Mn, Mo, Nb, Ti and Si were reduced, whereas the amount of oxidized Cr was increased compared to the NOT-AGED sample. The similar O 1s peak areas in Fig. 4(h) indicate the total amount of oxidized species on both samples is almost the same.

Besides Mn, the minor alloying elements (others than Fe and Cr) that showed decreased surface concentration at the AGED sample were the ones that were precipitated as $(FeCrSi)_2(MoNb)$-type Laves phase. Thus, the Laves particles bound these elements and prevented their diffusion to the surface. The decreased surface segregation and oxidation of Mn, on the other hand, is perfectly consistent with the oxidation experiment under ambient air conditions supporting the conclusion that $(FeCrSi)_2(MoNb)$-type Laves particles at the grain boundaries and dislocations had blocked the fast diffusion paths of Mn. The increased amount of oxidized Cr on the AGED sample in Fig. 4(b) suggests that normal lattice diffusion and oxidation of Cr compensates the reduced surface segregation and oxidation of minor alloying elements.

The O 1s spectra in Fig. 4(h) were fitted using two components centered at 531.1 and 532.5 eV corresponding to metal oxides (M–O, M = Fe, Cr, Mn, Mo, Nb, Ti) and oxidized Si (Si–O), respectively [33]. The higher intensity of the Si–O peak compared to the M–O peak in the NOT-AGED sample indicated that Si oxides were the dominant oxide species at the surface. If compared with the changes observed in the XP spectra of other elements, the Si–O to M–O peak ratio of the AGED sample was sharply decreased compared to the NOT-AGED sample suggesting that the oxidation of Si was strongly affected by the heat treatment.

The oxidation of Si deserved detailed attention because of its well-known property to dramatically increase the oxidation resistance of Fe–Cr alloys, even upon < 1% additions, by forming a near continuous amorphous SiO_2 at the oxide/metal interface which acts as a

diffusion barrier to the scale forming elements [1]. It has been proposed that Si-rich Laves phase particles can modify the morphology of this interfacial Si oxide layer [5]. Recently, we studied the temperature dependence of surface segregation on EN 1.4521 and showed that annealing a metallic surface at 650 °C in UHV induced strong surface segregation of Si and Nb, whereas annealing an oxidized surface in UHV at 650 °C resulted in strong surface enrichment of oxidized Mn and Cr together with Si and Nb [15]. In contrast, the surface segregation and oxidation of Ti required higher temperatures and was not significant at 650 °C. Therefore, the critical temperature of 650 °C was chosen for the in-depth analysis of early stages of surface oxidation.

Due to the distinct binding energy of O 1s peak of Si oxide compared to metal oxides, O 1s transition provided an ideal probe to study distribution of Si oxides in the oxide film. Fig. 5 depicts a more detailed surface analysis of the AGED sample after the oxygen exposure. Fig. 5(a) shows O 1s spectra recorded using three different photon energies facilitating a non-destructive depth profile analysis due to different kinetic energies of the photoemitted O 1s electrons. The Si–O to M–O peak intensity ratio increased as the information depth was decreased, which indicates that the Si oxides were localized closer to the surface compared to the metal oxides. The *surface sensitive* PEEM image in Fig. 4b and the *bulk sensitive* XAS-PEEM image of O K-edge in Fig. 4(d) show spatial distribution of oxidized Si (Si–O) [34] and metal oxides (M–O) [35,36].

According to the PEEM image in Fig. 5(b), the oxidized species were evenly distributed at the surface of individual grains with the exception of the locations of large Ti(CN) and

(NbTi)C particles. The XAS-PEEM image in Fig. 5(d) reveals strong M–O formation around the Ti(CN) and (NbTi)C particles but not inside the particles.

Strikingly, the XAS-PEEM images of Si–O and M–O in Fig. 5(d) have both similar contrast distribution with the Laves particles presented in Fig. 1 that suggests strong oxidation at the precipitate locations via inward oxygen diffusion. However, Si oxide was shown to form preferentially in the vicinity of the surface with more homogeneous spatial distribution which supports oxidation via outward lattice diffusion of Si. Fast surface segregation and oxidation of Si during the early stages of oxidation is perfectly commensurate with the formation of a protective oxide subscale at the oxide/metal interface to reduce the outward diffusion of scale forming elements (e.g. Cr and Mn) during the later stages of oxidation [1]. Furthermore, the deeper penetration of oxidation at the precipitate locations, including the Si-rich Laves particles, implicates the formation of particularly strong diffusion barrier at the locations that, without Laves precipitates, facilitate the fast diffusion of scale forming elements.

During the oxygen exposure in 5.3×10^{-5} Pa O_2 for 250 s at 650 °C a substantial amount of Cr had already oxidized and Si oxide had evenly covered the surface. In order to focus on the initial stages of Si oxidation, the pO_2 was further lowered and XPS measurements were conducted in real time. The Fig. 6(a) shows Si 2p spectra of an unoxidized surface and after different oxygen exposures at 650 °C for the AGED sample. The Si 2p spectra were fitted using two doublet peaks with doublet separation of 0.608 eV between the $2p_{3/2}$ and $2p_{1/2}$ levels of Si and the area branching ratio of 0.50. The $2p_{3/2}$ component binding energies of

102.6 eV and 103.7 eV correspond to Si oxidation states 3+ and 4+, respectively. All the oxygen exposures induced strong surface segregation and oxidation of Si. After the oxygen exposure in 5.3×10^{-5} Pa O_2 for 250 s (the same exposure was studied above in Figs. 4 and 5) Si was oxidized to both Si^{3+} and Si^{4+}. In contrast, after the oxygen exposure in 5.3×10^{-6} Pa O_2 for 250 s Si was primarily oxidized as Si^{3+}. The further decrease of pO_2 to 5.3×10^{-7} Pa did not change the oxidation state of Si but decreased the peak intensity due to kinetics of surface oxidation, albeit the oxidation time was increased to compensate the oxygen exposure.

Comparing the surface oxides after the oxygen exposures at 5.3×10^{-6} Pa and 5.3×10^{-7} Pa with that given at 5.3×10^{-5} Pa, the surface consists of increased amount of Nb, Ti and Al oxides in addition to Si oxides. However, Cr oxides were not formed. Thus, within the short oxygen exposures the oxygen induced surface segregation and oxidation of Si overcame the formation of Cr oxides. Therefore, the use of low pO_2 allowed the investigation of initial stages of interfacial Si oxidation before the formation of Cr rich oxide scale on top. Furthermore, at low pO_2 oxidation kinetics was slow enough to allow *operando* analysis of oxide film formation using surface sensitive PEEM.

Fig. 6(d) shows the evolution of Si–O PEEM intensity at different locations depicted in Fig. 6(b) during oxidation at 650 °C under oxygen pressure of 5.3×10^{-7} Pa. The presented data for submicrometer-sized Laves particles on three grains (A, B, C) are average values of tens of particles marked in Fig. 6(b). Fig. 6(c) shows the PEEM image of Si 2p (Si–O) at the end

of the oxygen exposure (oxidation time = 2500 s, Movie S1 includes all the PEEM images during oxidation and is available as supplementary material).

The PEEM measurement revealed strong lateral variations in the Si oxidation. Firstly, the Si oxide formation was strongly limited at the locations of Ti(CN)- and (NbTi)C-type precipitates. Secondly, the three grains showed different oxide growth rates. The Si oxide formation on grain C was significantly stronger than on grain A. Most strikingly, the Si oxide formation at Laves precipitates was significantly stronger than on the surrounding grain for all three grains (A, B, C). The Si oxidation proceeded initially fast at close to linear rate, which was followed by parabolic growth. Such a reaction kinetics indicates initial phase boundary process followed by diffusion control [37]. We emphasize to the reader that due to the surface sensitivity of the measurement, the Si–O PEEM intensity is not directly proportional to the amount of Si oxide on the surface at the later stages of the experiment when the oxidation may have proceeded deeper into the bulk phase.

Juuti et al. showed that the amount of Si in the Laves phase can vary between 6–10 at.% [21] that is significantly higher than the bulk concentration of Si (0.97 at.%). Thus, the increased Si oxidation rate at the Laves precipitate locations can be attributed to the higher Si concentration. Recently we studied segregation phenomena on the same EN 1.4521 steel under low pO_2 conditions and showed that surface segregation was favored to the <111> oriented grains [15]. Therefore, the different oxidation rates between grains A–C are most likely due to different grain orientations. Interestingly, Si oxide formation on grain C was

faster than at the Laves precipitate location on grain A that suggests that the grain orientation would be more dominant to the oxidation rate than the Si concentration.

Regardless of the fact that grain boundaries were enriched with Si-rich Laves phase [21], it was not possible to distinguish Si oxide enrichment at the grain boundaries by PEEM. Isik et al. showed using atom probe tomography that, besides bulky particles on grains, Laves phase forms as an elongated rod with a thickness of 10–20 nm along the grain boundaries [38]. Juuti et al. showed that the nucleation and growth of Laves particles at the grain boundaries were strongly affected by the thermal treatment history [21]. Preferential Si oxidation was observed at the grain boundaries of EN 1.4509 containing $(FeCrSi)_2Nb$-type Laves phase [39], but spherical submicron sized Laves particles at the grain boundaries of AGED EN 1.4509 were not found on the AGED EN 1.4521 sample (Fig. 1(a)). Therefore, it is evident that the apparent discrepancy was due to the resolution limit of the PEEM to distinguish oxidized Si at the narrow grain boundaries.

Based on the well-founded assumption that the $(FeCrSi)_2(MoNb)$ Laves phase forms at the grain boundaries and dislocations that, without Laves phase, provide fast diffusion path for oxide scale forming elements, it is clear that the preferential Si oxide formation at the Laves phase locations during the early stages of oxidation seals off the fast diffusion paths for the other scale forming elements. In particular, this mechanism was here shown to strongly limit the diffusion of Mn to the oxide scale. Even though Si was strongly enriched in the Laves phase, there was enough free Si to form continuous oxide film at the surface. Moreover, it is suggested that the randomly distributed Si oxide rich Laves precipitates at

the oxide scale/alloy interface can enhance the oxide scale adherence via pegging effect [40].

In addition to the precipitation effects also other diffusion processes during the heat treatment should be considered. Steel production involves high-temperature and forming processes which create defects, such as vacancies, to the alloy and these processes are too fast for the steel to equilibrate energetically. Diffusion can proceed via vacancies that are ubiquitous in α-Fe and numerous at the dislocations, grain boundaries and other interfaces. During the heat treatment substitutional (e.g. Cr, Mn, Nb, Si, Ti, P) and interstitial (e.g. C, N, O) elements will redistribute in an α-Fe alloy matrix to energetically more favorable positions. Recently Liu et al. studied the effects of dilute substitutional solutes and vacancies on the behaviors of C in α-Fe using ab-initio calculations [41]. The results revealed strong magnetic coupling between Mn and its nearest-neighboring Fe atoms assisted by Fe vacancy. This Mn-vacancy pair showed exceptionally strong bonding with interstitial C and acted as C trap. Therefore, it is reasonable to suggest that during the heat treatment diffusion of solute elements can fill in the vacancies by the Mn sites which may result in immobilized Mn.

The experiments in this study focused on the early stages of oxidation which precede the growth of a thickening Cr-rich oxide scale above the interfacial Si oxide layer. However, it is not possible to predict the degree of how much the $(FeCrSi)_2(MoNb)$ Laves phase precipitation can mitigate Mn diffusion kinetically upon longer time periods. It is suggested, though, that mobile Mo, Si and Nb in the alloy can fill in the vacancies

generated by the outward diffusion of Cr, and hence, continue restricting Mn diffusion. It became clear that the thermal history and Laves phase composition both had a strong effect on the oxidation properties that can be utilized in controlling the corrosion properties via heat treatments. For example, the Mo enrichment in the Laves phase is expected to affect corrosion properties at lower temperatures where Mo oxides are stable.

4. Conclusions

The influence of aging (120 h at 650 °C) on early stages of oxidation under ambient air conditions and at low pO_2 was studied on Ti–Nb stabilized ferritic stainless steel (EN 1.4521). The $(FeCrSi)_2(MoNb)$-type Laves phase induced by age-precipitation resulted in less pronounced surface segregation and oxidation of minor alloying elements at low pO_2. Si was shown to oxidize preferentially at the Laves precipitate locations via fast outward diffusion forming a diffusion barrier for the subsequent growth of the oxide scale. Furthermore, the *operando* analysis of Si oxidation revealed that grain orientation had stronger influence on oxidation rate than local Si concentration. Most significantly the age-precipitation of Laves phase limits the diffusion of Mn to the oxide scale under atmospheric conditions, and therefore, prevented the formation of low volatile $(Mn,Cr)_3O_4$ spinel oxide on Cr_2O_3. Thus, these results provide new insights to the interplay between microstructure and oxidation properties for ferritic stainless steels at high temperatures, which can be utilized to optimize the alloy composition and heat treatments of ferritic stainless steel to facilitate the growth of protective oxide scale with designed properties in terms of volatility and electrical conductivity.

Supplementary material

Details on surface analytical equipment, data acquisition and analysis are available as Supplementary material.

A movie file of operando analysis of Si oxidation during oxygen exposure at low pO_2 at 650 °C for the AGED EN 1.4521 is available as Supplementary Material.

Acknowledgments

The authors wish to acknowledge Mrs. Mirva Kujansuu and Mr. Jukka Säynäjäkangas (Outokumpu Stainless Oy) for providing the investigated stainless steel material. We are grateful to the staff of MAX IV Laboratory for the assistance during the measurements. This work was supported by the Academy of Finland (grant Nos. 141481, 286713, 141492, 283967, 273694, 309920 and 310359. H. A. was supported by the Jenny and Antti Wihuri Foundation. M. H. was supported by the Graduate School of Tampere University of Technology.

References

[1] J. Robertson, M.I. Manning, Healing layer formation in Fe–Cr–Si ferritic steels, Mater. Sci. Technol. 5 (1989) 741–753. doi:10.1179/mst.1989.5.8.741.

[2] C. Key, J. Eziashi, J. Froitzheim, R. Amendola, R. Smith, P. Gannon, Methods to Quantify Reactive Chromium Vaporization from Solid Oxide Fuel Cell Interconnects, J. Electrochem. Soc. 161 (2014) C373–C381. doi:10.1149/2.0041409jes.

[3] W. Wongpromrat, G. Berthomé, V. Parry, S. Chandra-ambhorn, W. Chandra-ambhorn, C. Pascal, A. Galerie, Y. Wouters, Reduction of chromium volatilisation from stainless steel interconnector of solid oxide electrochemical devices by controlled preoxidation, Corros. Sci. 106 (2016) 172–178. doi:10.1016/j.corsci.2016.02.002.

[4] S.P. Jiang, X. Chen, Chromium deposition and poisoning of cathodes of solid oxide fuel cells – A review, Int. J. Hydrog. Energy. 39 (2014) 505–531. doi:10.1016/j.ijhydene.2013.10.042.

[5] J.W. Fergus, Synergism in the design of interconnect alloy–coating combinations solid for oxide fuel cells, Scr. Mater. 65 (2011) 73–77. doi:10.1016/j.scriptamat.2010.09.020.

[6] Z. Zeng, K. Natesan, Z. Cai, S.B. Darling, The role of metal nanoparticles and nanonetworks in alloy degradation, Nat Mater. 7 (2008) 641–646. doi:10.1038/nmat2227.

[7] Y. Yamamoto, M.P. Brady, Z.P. Lu, P.J. Maziasz, C.T. Liu, B.A. Pint, K.L. More, H.M. Meyer, E.A. Payzant, Creep-Resistant, Al_2O_3-Forming Austenitic Stainless Steels, Science. 316 (2007) 433–436. doi:10.1126/science.1137711.

[8] M. Schütze, W.J. Quadakkers, Future Directions in the Field of High-Temperature Corrosion Research, Oxid. Met. (2017) 1–24. doi:10.1007/s11085-017-9719-3.

[9] K.H. Lo, C.H. Shek, J.K.L. Lai, Recent developments in stainless steels, Mater. Sci. Eng. R Rep. 65 (2009) 39–104. doi:10.1016/j.mser.2009.03.001.

[10] N. Mahato, A. Banerjee, A. Gupta, S. Omar, K. Balani, Progress in material selection for solid oxide fuel cell technology: A review, Prog. Mater. Sci. 72 (2015) 141–337. doi:10.1016/j.pmatsci.2015.01.001.

[11] E.D. Wachsman, K.T. Lee, Lowering the Temperature of Solid Oxide Fuel Cells, Science. 334 (2011) 935–939. doi:10.1126/science.1204090.

[12] M. Li, M. Zhao, F. Li, W. Zhou, V.K. Peterson, X. Xu, Z. Shao, I. Gentle, Z. Zhu, A niobium and tantalum co-doped perovskite cathode for solid oxide fuel cells operating below 500 °C, Nat. Commun. 8 (2017) 13990. doi:10.1038/ncomms13990.

[13] Y. Zhou, X. Guan, H. Zhou, K. Ramadoss, S. Adam, H. Liu, S. Lee, J. Shi, M. Tsuchiya, D.D. Fong, S. Ramanathan, Strongly correlated perovskite fuel cells, Nature. 534 (2016) 231–234. doi:10.1038/nature17653.

[14] D.J. Young, J. Zurek, L. Singheiser, W.J. Quadakkers, Temperature dependence of oxide scale formation on high-Cr ferritic steels in Ar–H_2–H_2O, Corros. Sci. 53 (2011) 2131–2141. doi:10.1016/j.corsci.2011.02.031.

[15] H. Ali-Löytty, M. Hannula, M. Honkanen, K. Östman, K. Lahtonen, M. Valden, Grain orientation dependent Nb–Ti microalloying mediated surface segregation on ferritic stainless steel, Corros. Sci. 112 (2016) 204–213. doi:10.1016/j.corsci.2016.07.024.

[16] L. Niewolak, A. Savenko, D. Grüner, H. Hattendorf, U. Breuer, W.J. Quadakkers, Temperature Dependence of Laves Phase Composition in Nb, W and Si-Alloyed High Chromium Ferritic Steels for SOFC Interconnect Applications, J. Phase Equilibria Diffus. 36 (2015) 471–484. doi:10.1007/s11669-015-0403-5.

[17] H. Ali-Löytty, P. Jussila, M. Valden, Optimization of the electrical properties of Ti–Nb stabilized ferritic stainless steel SOFC interconnect alloy upon high-temperature oxidation: The role of excess Nb on the interfacial oxidation at the oxide–metal interface, Int. J. Hydrog. Energy. 38 (2013) 1039–1051.

[18] T. Horita, Y. Xiong, K. Yamaji, H. Kishimoto, N. Sakai, M.E. Brito, H. Yokokawa, Imaging of mass transports around the oxide scale/Fe-Cr alloy interfaces, Solid State Ion. 174 (2004) 41–48. doi:10.1016/j.ssi.2004.07.040.

[19] T. Horita, H. Kishimoto, K. Yamaji, Y. Xiong, N. Sakai, M.E. Brito, H. Yokokawa, Evaluation of Laves-phase forming Fe–Cr alloy for SOFC interconnects in reducing atmosphere, J. Power Sources. 176 (2008) 54–61. doi:10.1016/j.jpowsour.2007.10.041.

[20] R.E. Lobnig, H.P. Schmidt, K. Hennesen, H.J. Grabke, Diffusion of cations in chromia layers grown on iron-base alloys, Oxid. Met. 37 (1992) 81–93. doi:10.1007/BF00665632.

[21] T. Juuti, L. Rovatti, A. Mäkelä, L.P. Karjalainen, D. Porter, Influence of long heat treatments on the laves phase nucleation in a type 444 ferritic stainless steel, J. Alloys Compd. 616 (2014) 250–256. doi:10.1016/j.jallcom.2014.06.201.

[22] G.R. Speich, Precipitation of Laves phases from iron-niobium (columbium) and iron-titanium solid solutions, Trans Met. Soc AIME. 224 (1962) 850–858.

[23] M.I. Isik, A. Kostka, V.A. Yardley, K.G. Pradeep, M.J. Duarte, P.P. Choi, D. Raabe, G. Eggeler, The nucleation of Mo-rich Laves phase particles adjacent to $M_{23}C_6$ micrograin boundary carbides in 12% Cr tempered martensite ferritic steels, Acta Mater. 90 (2015) 94–104. doi:10.1016/j.actamat.2015.01.027.

[24] S. Swaminathan, C. Mallika, N.G. Krishna, C. Thinaharan, T. Jayakumar, U. Kamachi Mudali, Evolution of surface chemistry and morphology of oxide scale formed during initial stage oxidation of modified 9Cr–1Mo steel, Corros. Sci. 79 (2014) 59–68. doi:10.1016/j.corsci.2013.10.026.

[25] L. Cooper, S. Benhaddad, A. Wood, D.G. Ivey, The effect of surface treatment on the oxidation of ferritic stainless steels used for solid oxide fuel cell interconnects, J. Power Sources. 184 (2008) 220–228. doi:10.1016/j.jpowsour.2008.06.010.

[26] T. Horita, K. Yamaji, H. Yokokawa, A. Toji, T. Uehara, K. Ogasawara, H. Kameda, Y. Matsuzaki, S. Yamashita, Effects of Si and Al concentrations in Fe–Cr alloy on the formation of oxide scales in H2–H2O, Int. J. Hydrog. Energy. 33 (2008) 6308–6315. doi:10.1016/j.ijhydene.2008.07.118.

[27] N.J. Magdefrau, L. Chen, E.Y. Sun, M. Aindow, Effects of alloy heat treatment on oxidation kinetics and scale morphology for Crofer 22 APU, J. Power Sources. 241 (2013) 756–767. doi:10.1016/j.jpowsour.2013.03.181.

[28] N.K. Othman, J. Zhang, D.J. Young, Temperature and water vapour effects on the cyclic oxidation behaviour of Fe–Cr alloys, Corros. Sci. 52 (2010) 2827–2836. doi:10.1016/j.corsci.2010.04.026.

[29] M. Palcut, L. Mikkelsen, K. Neufeld, M. Chen, R. Knibbe, P.V. Hendriksen, Corrosion stability of ferritic stainless steels for solid oxide electrolyser cell interconnects, Corros. Sci. 52 (2010) 3309–3320. doi:10.1016/j.corsci.2010.06.006.

[30] J. Froitzheim, G.H. Meier, L. Niewolak, P.J. Ennis, H. Hattendorf, L. Singheiser, W.J. Quadakkers, Development of high strength ferritic steel for interconnect application in SOFCs, J. Power Sources. 178 (2008) 163–173. doi:10.1016/j.jpowsour.2007.12.028.

[31] A. Jacob, C. Schmetterer, D. Grüner, E. Wessel, B. Hallstedt, L. Singheiser, The Cr–Fe–Nb ternary system: Experimental isothermal sections at 700 °C, 1050 °C and 1350 °C, J. Alloys Compd. 648 (2015) 168–177. doi:10.1016/j.jallcom.2015.06.137.

[32] Z. Yang, Recent advances in metallic interconnects for solid oxide fuel cells, Int. Mater. Rev. 53 (2008) 39–54. doi:10.1179/174328007X212526.

[33] A.V. Naumkin, A. Kraut-Vass, C.P. J, NIST XPS Database 20, 2008. http://srdata.nist.gov/xps/.

[34] B.T. Poe, C. Romano, G. Henderson, Raman and XANES spectroscopy of permanently densified vitreous silica, J. Non-Cryst. Solids. 341 (2004) 162–169. doi:10.1016/j.jnoncrysol.2004.04.014.

[35] J.G. Chen, NEXAFS investigations of transition metal oxides, nitrides, carbides, sulfides and other interstitial compounds, Surf. Sci. Rep. 30 (1997) 1–152. doi:10.1016/S0167-5729(97)00011-3.

[36] F.M.F. de Groot, M. Grioni, J.C. Fuggle, J. Ghijsen, G.A. Sawatzky, H. Petersen, Oxygen 1s x-ray-absorption edges of transition-metal oxides, Phys. Rev. B. 40 (1989) 5715–5723. doi:10.1103/PhysRevB.40.5715.

[37] D.J. Young, High temperature oxidation and corrosion of metals, Elsevier, Oxford, UK, 2008.

[38] M.I. Isik, A. Kostka, G. Eggeler, On the nucleation of Laves phase particles during high-temperature exposure and creep of tempered martensite ferritic steels, Acta Mater. 81 (2014) 230–240. doi:10.1016/j.actamat.2014.08.008.

[39] H. Ali-Löytty, P. Jussila, T. Juuti, L.P. Karjalainen, A.A. Zakharov, M. Valden, Influence of precipitation on initial high-temperature oxidation of Ti–Nb stabilized ferritic stainless steel SOFC interconnect alloy, Int. J. Hydrog. Energy. 37 (2012) 14528–14535. doi:10.1016/j.ijhydene.2012.07.097.

[40] H. Buscail, S.E. Messki, F. Riffard, S. Perrier, R. Cueff, E. Caudron, C. Issartel, Characterization of the oxides formed at 1000 °C on the AISI 316L stainless steel—Role of molybdenum, Mater. Chem. Phys. 111 (2008) 491–496. doi:10.1016/j.matchemphys.2008.04.054.

[41] P. Liu, W. Xing, X. Cheng, D. Li, Y. Li, X.-Q. Chen, Effects of dilute substitutional solutes on interstitial carbon in α-Fe: Interactions and associated carbon diffusion from first-principles calculations, Phys. Rev. B. 90 (2014) 24103. doi:10.1103/PhysRevB.90.024103.

Figure captions

Fig. 1. (a) SE image, (b) Nb M_3-edge and (c) Ti L_3-edge XAS-PEEM images of AGED (120 h at 650 °C) EN 1.4521 sample. The labels in (a) indicate the locations of three grains (A, B, C) and different precipitates the properties of which have been investigated in the present study. (For interpretation of the references to colour in this figure legend, the reader is referred to the web version of this article.)

Fig. 2. XPS analysis of NOT-AGED and AGED (120 h at 650 °C) EN 1.4521 after 30 min oxidation in ambient air at 650 °C. (a) Mn 2p transitions, (b,d) SE images and (c,e) overlaid PEEM images of Mn (blue), Fe (red) and Cr (green) oxides measured from the same positions as the SE images. (For interpretation of the references to colour in this figure legend, the reader is referred to the web version of this article.)

Fig. 3. XPS depth profiles showing oxygen and oxidized components of Fe, Cr, Mn, Mo, Si and Nb for (a) NOT-AGED and (b) AGED (120 h at 650 °C) EN 1.4521 after 30 min oxidation in ambient air at 650 °C. Oxide–metal interface has been determined according to the oxygen concentration. (For interpretation of the references to colour in this figure legend, the reader is referred to the web version of this article.)

Fig. 4. XP spectra of (a) Fe 2p, (b) Cr 2p, (c) Mn 2p, (d) Mo 3d, (e) Nb 3d, (f) Ti 2p, (g) Si 2p and (h) O 1s for NOT-AGED and AGED (120 h at 650 °C) EN 1.4521 after oxygen exposure in 5.3×10^{-5} Pa O_2 for 250 s at 650 °C. Before oxygen exposures the samples were sputter cleaned and annealed for 5 min at 650 °C in UHV. The spectra are aligned

with their backgrounds, which allows surface concentration of elements to be directly compared with the samples. The presented binding energy values are based on fitted Gaussian–Lorentzian lineshapes and, in the case of doublet transitions, correspond to their $p_{3/2}$ or $d_{5/2}$ components. The minor alloying elements (others than Fe and Cr) that had precipitated as Laves phase in the AGED sample are marked with L. (For interpretation of the references to colour in this figure legend, the reader is referred to the web version of this article.)

Fig. 5. AGED (120 h at 650 °C) EN 1.4521 after oxygen exposure in 5.3×10^{-5} Pa O_2 for 250 s at 650 °C. (a) O 1s transition measured with three different photon energies corresponding to different information depths. The inset depicts the relative concentration of oxidized Si (Si–O) as a function of information depth. (b) Overlaid surface sensitive PEEM images of oxidized metals (M–O) and oxidized silicon (Si–O) as determined from the chemical state resolved O 1s image. The O 1s PEEM image was acquired using an incident photon energy of 580 eV corresponding to an information depth of 1.6 nm. (c) O K-edge XAS spectra measured at the location of Ti(CN) and (NbTi)C precipitates (—) and over the grains (—). (d) Overlaid bulk sensitive O K-edge XAS-PEEM images of oxidized metals (M–O) and oxidized silicon (Si–O) recorded at the same position with (b). The energy positions of M–O (533 eV) and Si–O (539 eV) XAS-PEEM images are depicted in (c). The information depth of the XAS measurements is >10 nm. The measured area and labeled grains in (b, d) correspond to those of Fig. 1. (For interpretation of the references to colour in this figure legend, the reader is referred to the web version of this article.)

Fig. 6. (a) XP spectra of Si 2p for AGED (120 h at 650 °C) EN 1.4521 after sputter cleaning and annealing for 5 min at 650 °C (unoxidized), and after oxygen exposures in 5.3 $\times$ 10^{-5} Pa O_2 for 250 s, 5.3 $\times$ 10^{-6} Pa O_2 for 250 s and 5.3 $\times$ 10^{-7} Pa O_2 for 2500 s at 650 °C. (b) SE image of the sample showing precipitate and grain locations. (c) PEEM image of Si 2p (Si–O) transition after oxygen exposure in 5.3 $\times$ 10^{-7} Pa O_2 for 2500 s at 650 °C. (d) Spatially resolved evolution of Si–O PEEM intensity recorded in *operando* during oxidation at 650 °C under oxygen pressure of 5.3 $\times$ 10^{-7} Pa. The solid lines in (d) are quartic polynomial fits to the data. The different locations are shown in (b) and they correspond to those of Fig. 1. The XPS and PEEM data were acquired using an incident photon energy of 150 eV corresponding to an information depth of 1.6 nm. (For interpretation of the references to colour in this figure legend, the reader is referred to the web version of this article.)

Table

Table 1. Bulk composition and calculated equilibrium composition at 650 °C for the investigated EN 1.4521 steel. In addition to the tabulated elements, the alloy contains very low concentrations of other minor and trace elements such as Cu (0.20 at.%), Al (0.01 at.%), P and Sn.

at.%	Fe	Cr	Mo	Si	Mn	Ni	Nb	Ti	C	N	Mole fraction (%)
Bulk composition	77.60	18.60	1.17	0.97	0.50	0.24	0.22	0.14	0.06	0.05	100.00
Equilibrium composition at 650 °C											
bcc	77.21	18.59	1.12	0.92	0.50	0.24	0.01	0.06	0.00	0.00	99.09
Laves	57.70	2.00	7.60	6.90	0.00	0.02	25.80	0.02			0.68
Ti(CN)								50.11	13.85	36.04	0.14
(NbTi)C							44.49	8.59	46.83		0.09

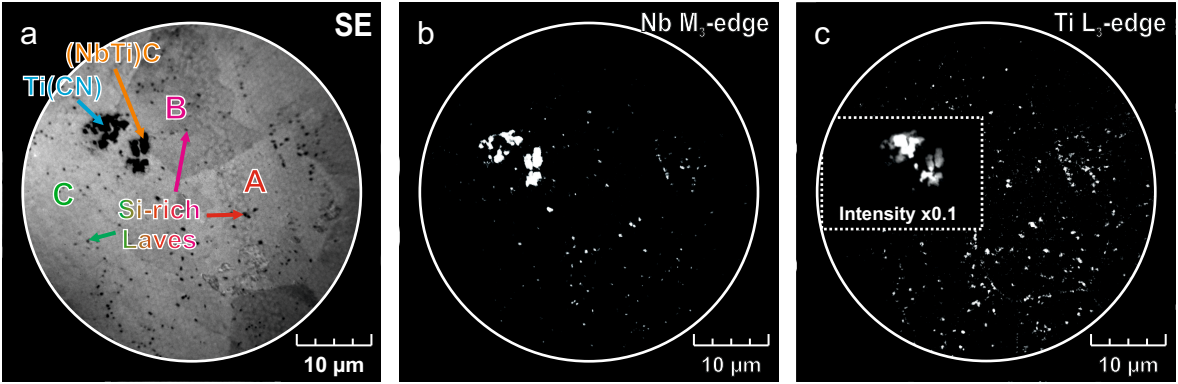
a
SE
(NbTi)C
Ti(CN)
B
A
C
Si-rich
Laves
10 μm
b
Nb M3-edge
10 μm
c
Ti L3-edge
Intensity x0.1
10 μm

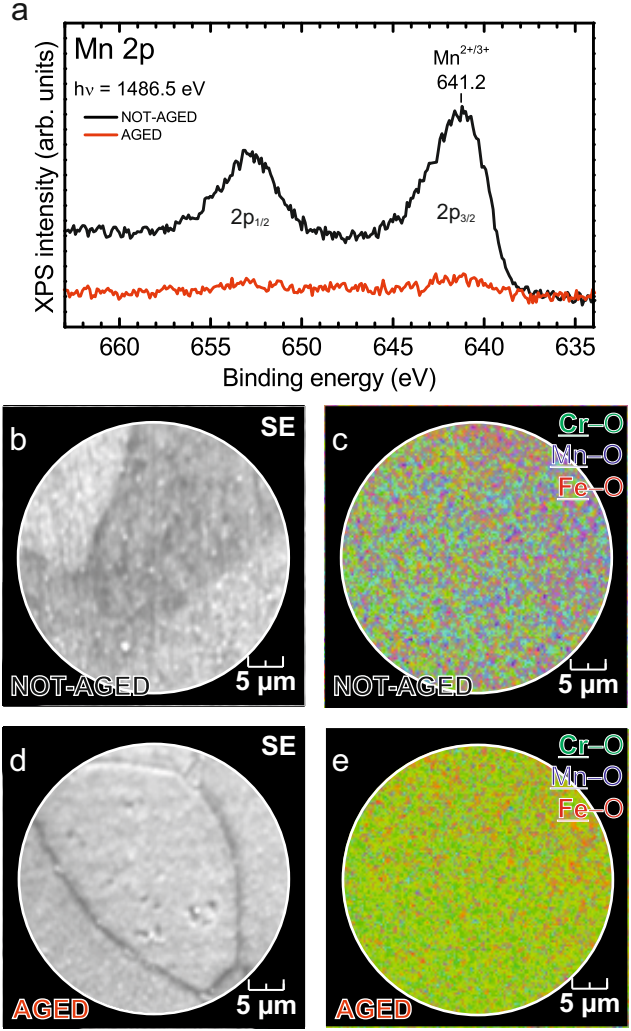
a
Mn 2p
hν = 1486.5 eV
NOT-AGED
AGED
Mn2+/3+
641.2
2p1/2
2p3/2
XPS intensity (arb. units)
660
655
650
645
640
635
Binding energy (eV)
b
SE
NOT-AGED
5 μm
c
Cr–O
Mn–O
Fe–O
NOT-AGED
5 μm
d
SE
AGED
5 μm
e
Cr–O
Mn–O
Fe–O
AGED
5 μm

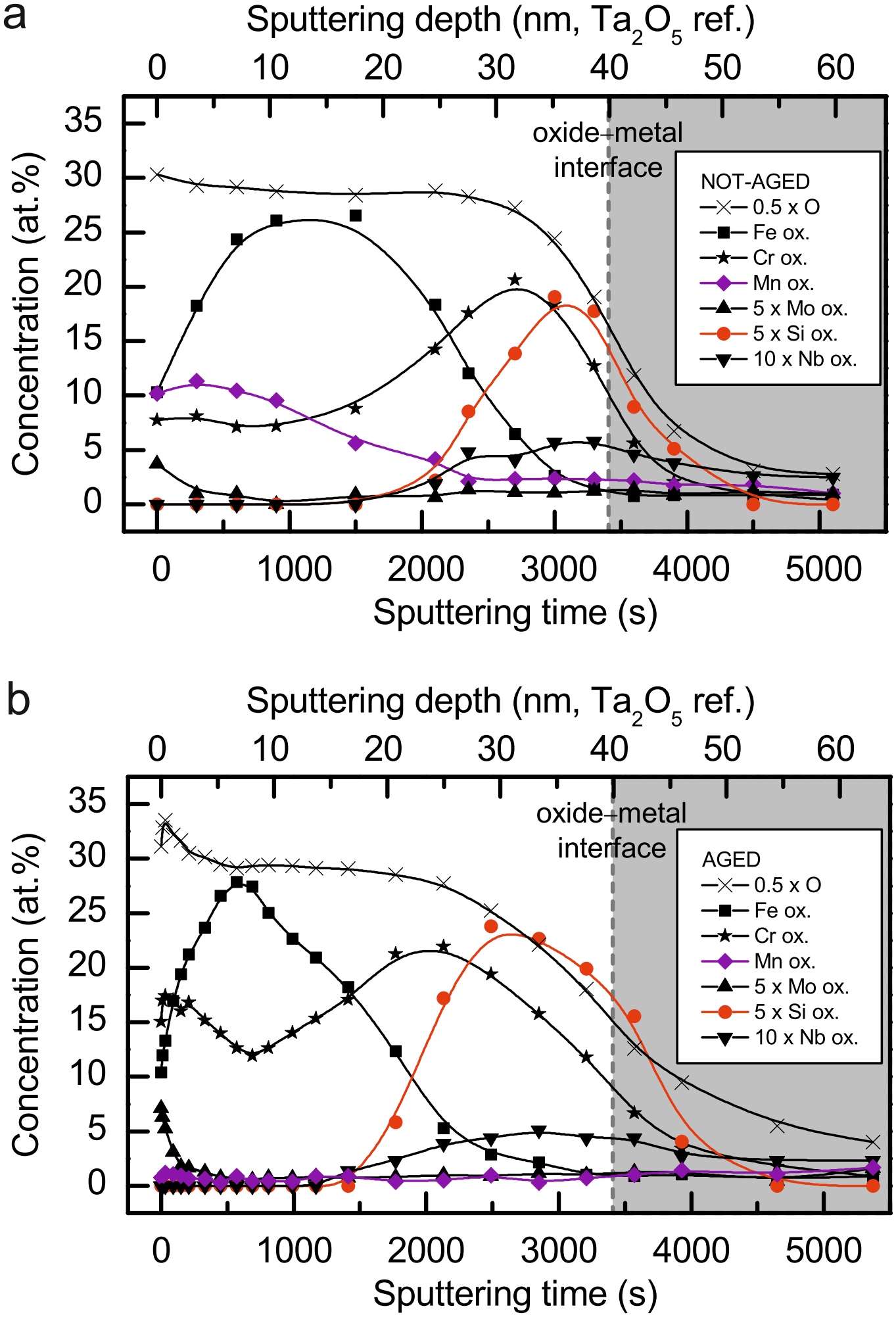
a
Sputtering depth (nm, Ta2O5 ref.)
0
10
20
30
40
50
60
oxide–metal
interface
NOT-AGED
0.5 x O
Fe ox.
Cr ox.
Mn ox.
5 x Mo ox.
5 x Si ox.
10 x Nb ox.
Concentration (at.%)
35
30
25
20
15
10
5
0
0
1000
2000
3000
4000
5000
Sputtering time (s)
b
Sputtering depth (nm, Ta2O5 ref.)
0
10
20
30
40
50
60
oxide–metal
interface
AGED
0.5 x O
Fe ox.
Cr ox.
Mn ox.
5 x Mo ox.
5 x Si ox.
10 x Nb ox.
Concentration (at.%)
35
30
25
20
15
10
5
0
0
1000
2000
3000
4000
5000
Sputtering time (s)

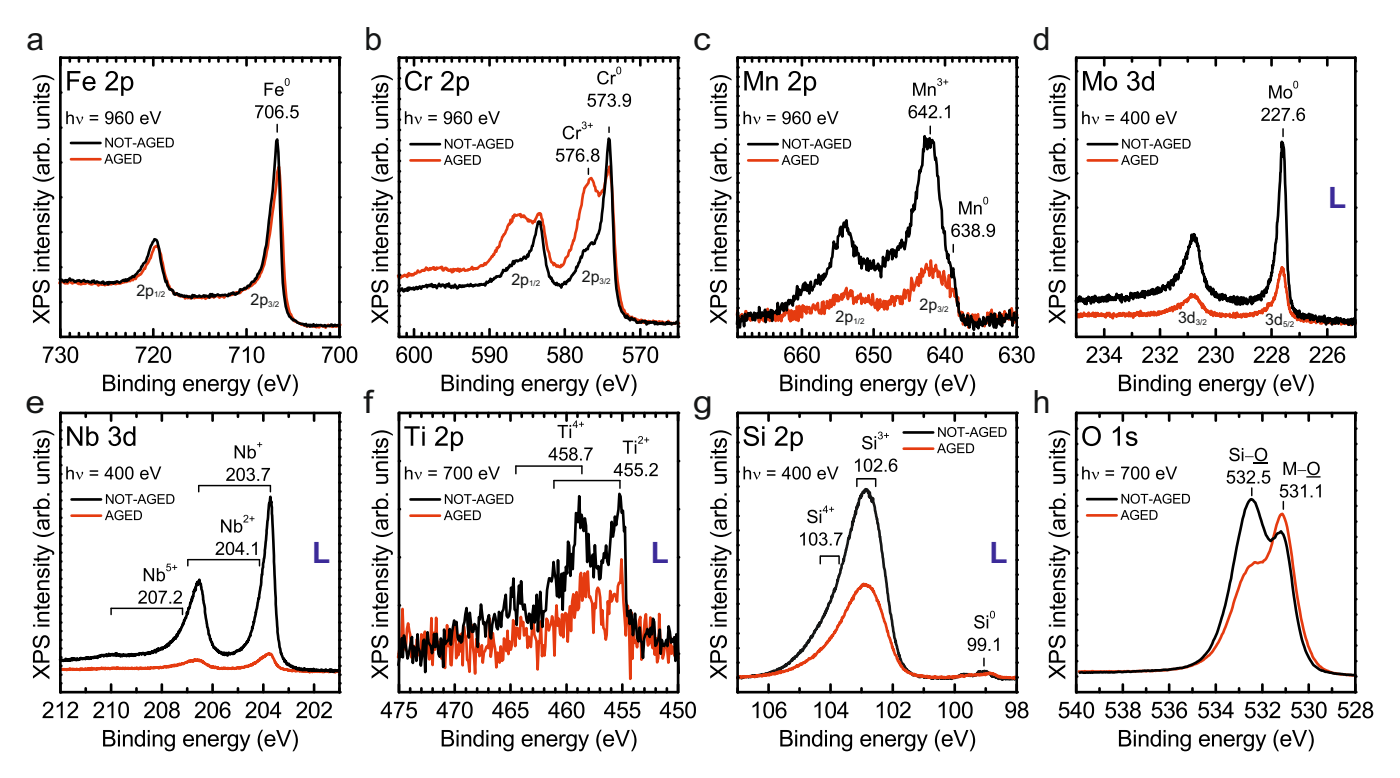
a
Fe 2p
hν = 960 eV
NOT-AGED
AGED
Fe0
706.5
2p1/2
2p3/2
XPS intensity (arb. units)
Binding energy (eV)
b
Cr 2p
hν = 960 eV
Cr0
573.9
Cr3+
576.8
2p1/2
2p3/2
c
Mn 2p
hν = 960 eV
Mn3+
642.1
Mn0
638.9
d
Mo 3d
hν = 400 eV
Mo0
227.6
L
3d3/2
3d5/2
e
Nb 3d
hν = 400 eV
Nb+
203.7
Nb2+
204.1
Nb5+
207.2
f
Ti 2p
hν = 700 eV
Ti4+
458.7
Ti2+
455.2
g
Si 2p
hν = 400 eV
Si3+
102.6
Si4+
103.7
Si0
99.1
h
O 1s
hν = 700 eV
Si–O
532.5
M–O
531.1

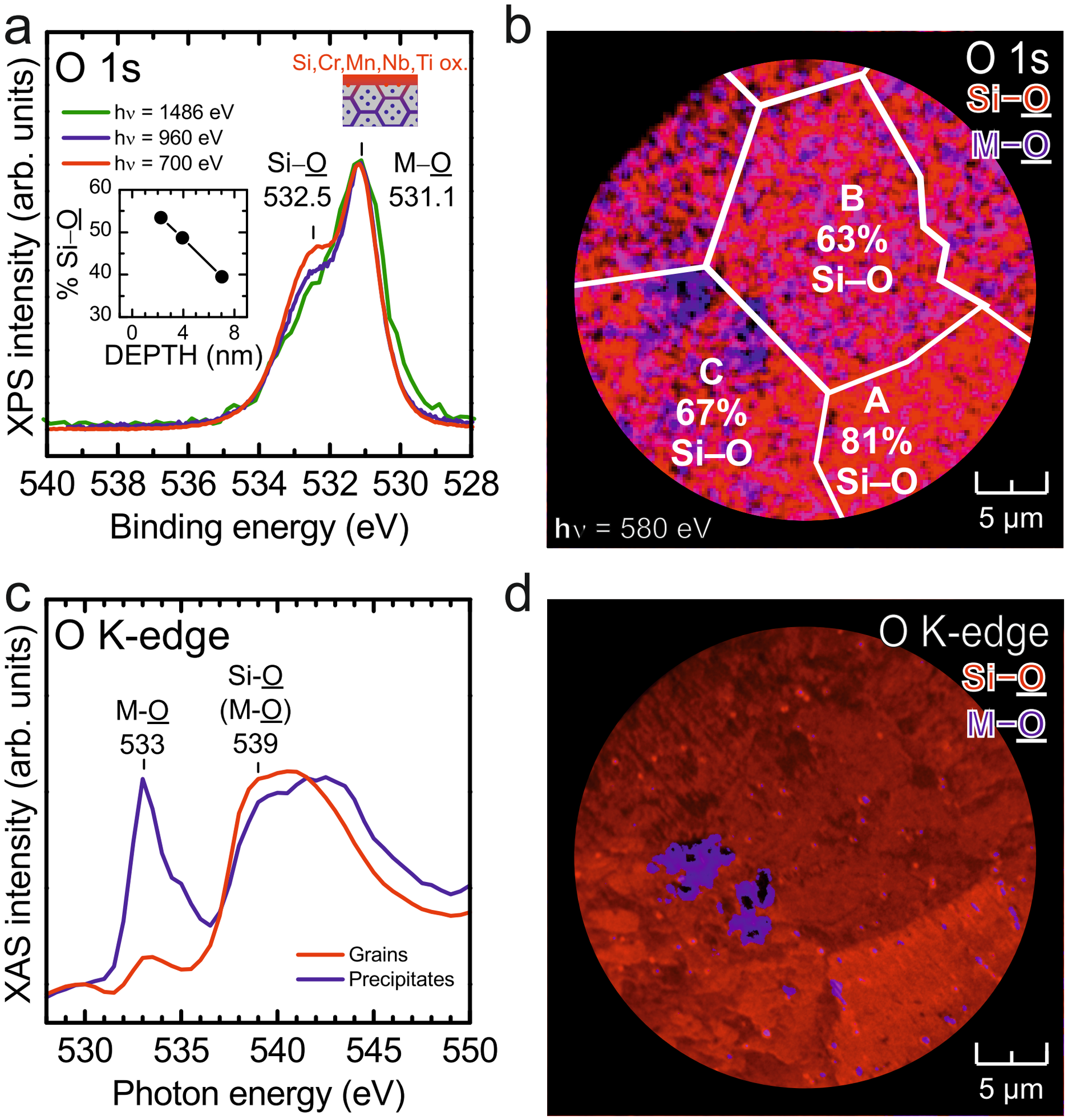
a
O 1s
Si,Cr,Mn,Nb,Ti ox.
hν = 1486 eV
hν = 960 eV
hν = 700 eV
Si–O
532.5
M–O
531.1
% Si–O
60
50
40
30
0
4
8
DEPTH (nm)
XPS intensity (arb. units)
540 538 536 534 532 530 528
Binding energy (eV)
b
O 1s
Si–O
M–O
B
63%
Si–O
C
67%
Si–O
A
81%
Si–O
hν = 580 eV
5 μm
c
O K-edge
M-O
533
Si-O
(M-O)
539
Grains
Precipitates
XAS intensity (arb. units)
530 535 540 545 550
Photon energy (eV)
d
O K-edge
Si–O
M–O
5 μm

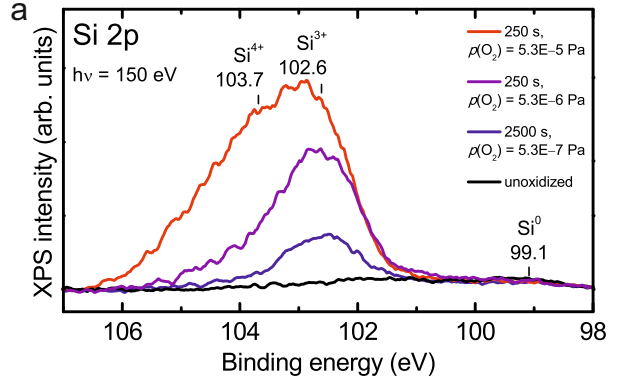
a
Si 2p
hν = 150 eV
Si4+
103.7
Si3+
102.6
250 s,
p(O2) = 5.3E–5 Pa
250 s,
p(O2) = 5.3E–6 Pa
2500 s,
p(O2) = 5.3E–7 Pa
unoxidized
Si0
99.1
XPS intensity (arb. units)
106
104
102
100
98
Binding energy (eV)

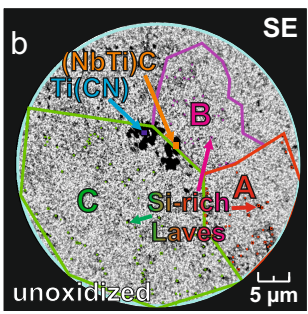
b
SE
(NbTi)C
Ti(CN)
B
C
Si-rich
Laves
A
unoxidized
5 µm

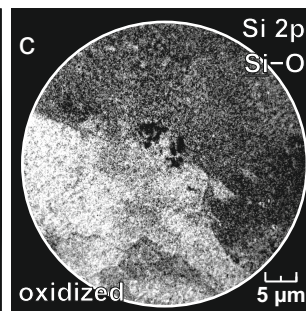
c
Si 2p
Si–O
oxidized
5 µm

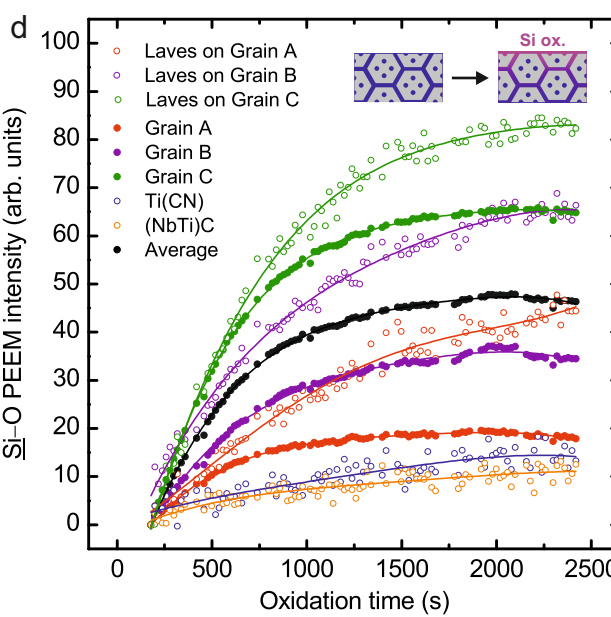
d
Laves on Grain A
Laves on Grain B
Laves on Grain C
Grain A
Grain B
Grain C
Ti(CN)
(NbTi)C
Average
Si ox.
Si–O PEEM intensity (arb. units)
0
10
20
30
40
50
60
70
80
90
100
0
500
1000
1500
2000
2500
Oxidation time (s)

Supplementary material:

The role of $(FeCrSi)_2(MoNb)$-type Laves phase on the formation of Mn-rich protective oxide scale on ferritic stainless steel

Harri Ali-Löytty[a], Markku Hannula[a], Timo Juuti[b], Yuran Niu[c], Alexei A. Zakharov[c], and Mika Valden[a]

[a]Surface Science Group, Laboratory of Photonics, Tampere University of Technology, P.O. Box 692, FI-33101 Tampere, Finland

[b]Centre for Advanced Steels Research, University of Oulu, P.O.B. 4200, FI-90014 Oulu, Finland

[c]MAX IV Laboratory, Lund University, P.O. Box 118, SE-22100 Lund, Sweden

Experimental

Surface analytical equipment

PEEM measurements employing laboratory photon sources were carried out using a NanoESCA (Omicron NanoTechnology GmbH) spectromicroscopy system (Finnish research infrastructure, FIRI: NanoMAT Laboratory) [2]. Monochromatized focused Al Kα radiation (hν = 1486.5 eV, ULVAC-PHI model 36-100 Focused X-ray source) was utilized for core level spectroscopy and imaging, whereas, secondary electron (SE) images were measured with Hg UV-source (Focus GmbH). The XPS depth profiling was carried out in a multi-technique surface analysis system, which has been described in detail elsewhere (see Ref. [3]). The spectra were excited by non-monochromatized Al Kα radiation and recorded using hemispherical VG Microtech CLAM4 MCD LNo5 electron analyzer. Depth profiling was accomplished by alternating cycles of 2.5 keV Ar^+ ion sputtering and XPS measurements. Sputtering rate of 0.012 nm s^{-1} was determined for a Ta_2O_5 reference material (BCR-261T). The XPS, PEEM, XAS-PEEM and SE image measurements employing synchrotron radiation were performed at the soft X-ray beamline I311 in the synchrotron radiation facility MAX IV Laboratory, Sweden (FIRI: MAX IV Laboratory). The beamline has been described in Ref. [4]. In short, I311 is an undulator beamline with a modified SX-700 monochromator and two endstations. High-resolution XPS measurement were conducted in the spectroscopy endstation equipped with a hemispherical SCIENTA SES-200 electron analyzer. PEEM, XAS-PEEM and SE image measurements were conducted in the microscopy endstation with a spectroscopic photoemission and low-energy electron microscope (SPELEEM) III [5] (Elmitec GmbH). The analysis area in all XPS setups was large in comparison to the average grain size of the sample; therefore, the XPS spectra represent surface analysis over a large number of individual grains.

Data analysis

The chemical states of elements were determined from XPS spectra by least-squares fitting of asymmetric Gaussian–Lorentzian lineshapes to the photoelectron peaks after subtracting

a Shirley background. The inelastic electron background subtraction from the core-level PEEM images was done by subtracting an image measured off the peak. During the *operando* experiment PEEM images were recorded with 20 s exposure time alternating between the peak position and the background. Recorded PEEM images were corrected for thermal drift before the background subtraction. XAS-PEEM images were analyzed by subtracting an image recorded at the pre-edge position from the image recorded at the absorption edge. The analysis of PEEM and XAS-PEEM data was accomplished by using ImageJ software (version 1.50b). The XPS data analysis was made by using CasaXPS software (version 2.3.16) [6], and Scofield photoionization cross-sections were used for the determination of atomic concentrations (hν = 1486.5 eV) [7]. The binding energy scale was calibrated either with the metallic Fe $2p_{3/2}$ peak set to 706.5 eV (hν = 1486.5 eV) or according to the Fermi edge.

Information depth

The XPS data was acquired using the optimized surface sensitivity by selecting a transition specific incident photon energy. The XPS information depth is determined by the electron inelastic mean free path (IMFP, λ) which depends on the kinetic energy of the photoelectrons. In general, the XPS information depth at normal emission (3λ) for a given transition decreases with decreasing photon energy and has the minimum value at electron kinetic energies (E_K) of 30–100 eV. For example, in the case of O 1s the information depth is reduced from 7.0 nm (hν = 1486 eV; E_K = 955 eV) to 1.6 nm (hν = 580 eV; E_K = 49 eV), as determined by the TPP-2M equation for the SiO_2 medium [8]. Due to the very low energy of the secondary electrons (less than 10 eV) that gives contrast to the XAS-PEEM images and the increase of the IMFP at very low energy, XAS-PEEM is here considered a bulk sensitive method with the information depth of >10 nm. It is worth noting that the information depth of common energy-dispersive X-ray spectroscopy analysis is typically >1000 nm.

References

[1] T. Juuti, L. Rovatti, A. Mäkelä, L.P. Karjalainen, D. Porter, Influence of long heat treatments on the laves phase nucleation in a type 444 ferritic stainless steel, J. Alloys Compd. 616 (2014) 250–256. doi:10.1016/j.jallcom.2014.06.201.

[2] O. Renault, M. Lavayssière, A. Bailly, D. Mariolle, N. Barrett, Core level photoelectron spectromicroscopy with Al Kα1 excitation at 500 nm spatial resolution, J. Electron Spectrosc. Relat. Phenom. 171 (2009) 68–71. doi:10.1016/j.elspec.2009.03.008.

[3] K. Lahtonen, M. Lampimaki, P. Jussila, M. Hirsimaki, M. Valden, Instrumentation and analytical methods of an x-ray photoelectron spectroscopy–scanning tunneling microscopy surface analysis system for studying nanostructured materials, Rev. Sci. Instrum. 77 (2006) 83901. doi:10.1063/1.2221539.

[4] R. Nyholm, J.N. Andersen, U. Johansson, B.N. Jensen, I. Lindau, Beamline I311 at MAX-LAB: a VUV/soft X-ray undulator beamline for high resolution electron spectroscopy, Nucl. Instrum. Methods Phys. Res. Sect. Accel. Spectrometers Detect. Assoc. Equip. 467–468 (2001) 520–524. doi:10.1016/S0168-9002(01)00399-0

[5] See www.elmitec.de for details of the SPELEEM III instrument manufactured by Elmitec GmbH.

[6] N. Fairley, CasaXPS: Spectrum Processing Software for XPS, AES and SIMS, 2011. http://www.casaxps.com/.

[7] J.H. Scofield, Hartree-Slater subshell photoionization cross-sections at 1254 and 1487 eV, J. Electron Spectrosc. Relat. Phenom. 8 (1976) 129–137. doi:10.1016/0368-2048(76)80015-1.

[8] S. Tanuma, C.J. Powell, D.R. Penn, Calculations of electron inelastic mean free paths. V. Data for 14 organic compounds over the 50–2000 eV range, Surf. Interface Anal. 21 (1994) 165–176. doi:10.1002/sia.740210302.

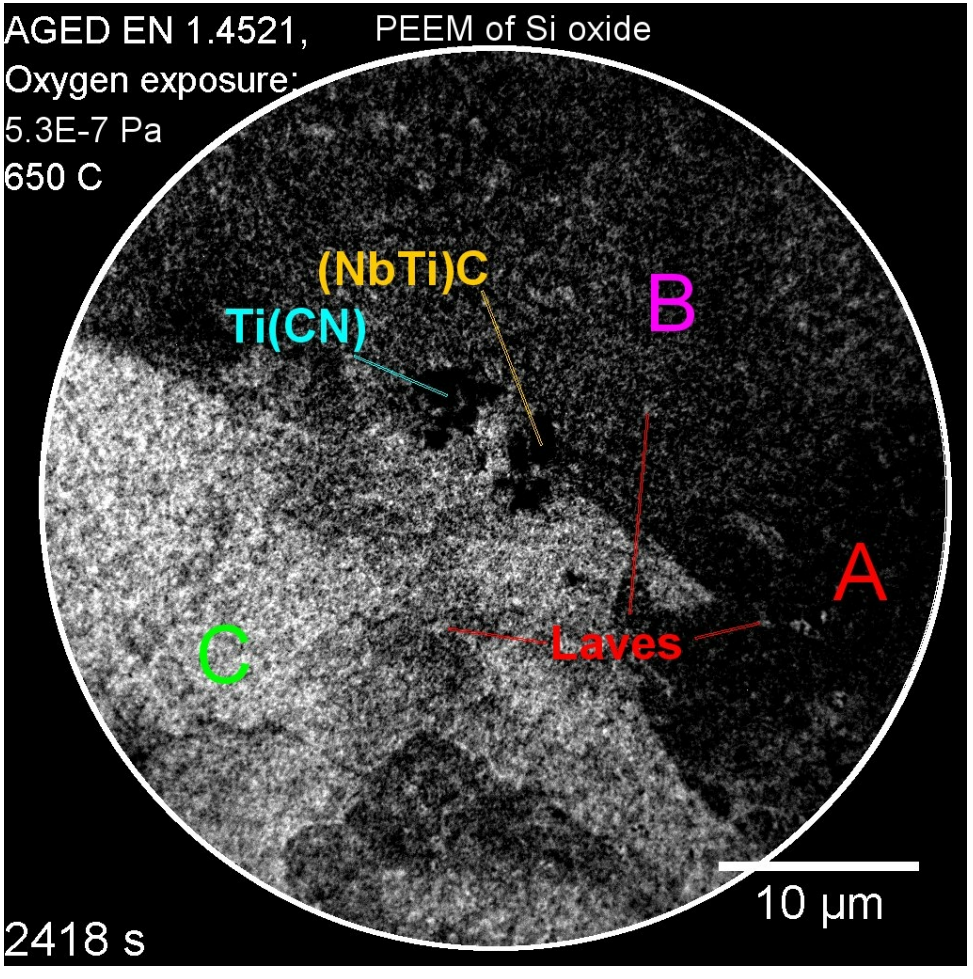
AGED EN 1.4521,
Oxygen exposure:
5.3E-7 Pa
650 C
PEEM of Si oxide
(NbTi)C
Ti(CN)
B
A
C
Laves
10 µm
2418 s

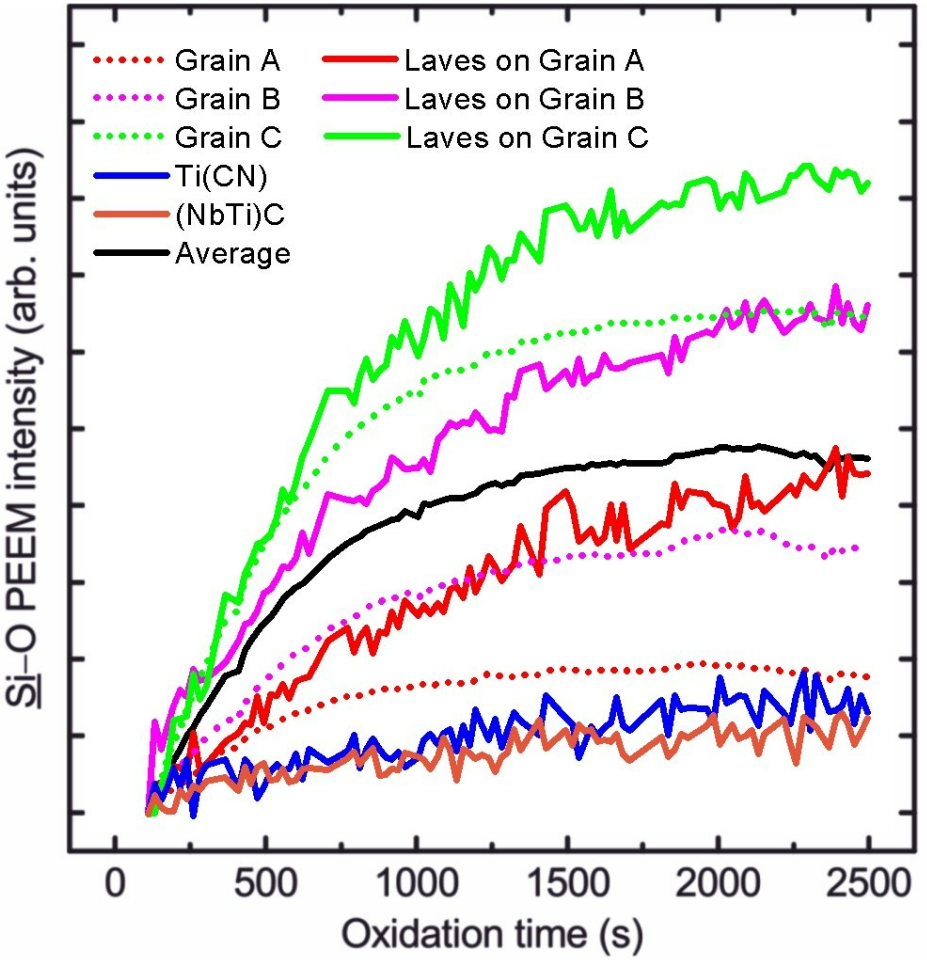
Grain A
Grain B
Grain C
Ti(CN)
(NbTi)C
Average
Laves on Grain A
Laves on Grain B
Laves on Grain C
Si–O PEEM intensity (arb. units)
0
500
1000
1500
2000
2500
Oxidation time (s)